HOKKAIDO UNIVERSITY

Title	Empirical Bayes method using surrounding pixel information for number and brightness analysis
Author(s)	Fukushima, Ryosuke; Yamamoto, Johtaro; Kinjo, Masataka
Citation	Biophysical journal, 120(11), 2156-2171 https://doi.org/10.1016/j.bpj.2021.03.033
Issue Date	2021-06-01
Doc URL	http://hdl.handle.net/2115/85665
Rights	©2021. This manuscript version is made available under the CC-BY-NC-ND 4.0 license http://creativecommons.org/licenses/by-nc-nd/4.0/
Rights(URL)	http://creativecommons.org/licenses/by-nc-nd/4.0/
Type	article (author version)
Additional Information	There are other files related to this item in HUSCAP. Check the above URL.
File Information	Biophys. J. 120-11_2156-2171.pdf

Title

Empirical Bayes Method Using Surrounding Pixel Information for Number and Brightness Analysis

Author Names

Ryosuke Fukushima[1], Johtaro Yamamoto[2, 3], Masataka Kinjo[3, *]

*Correspondence

E-mail address: kinjo@sci.hokudai.ac.jp

Affiliations

[1]Laboratory of Molecular Cell Dynamics, Graduate School of Life Science, Hokkaido University, Kita-21 Nishi-11, Kita-ku, Sapporo, Hokkaido 001-0021, Japan

[2]Health and Medical Research Institute, National Institute of Advanced Industrial Science and Technology (AIST), Central 6, 1-1-1 Higashi, Tsukuba, Ibaraki 305-8566, Japan

[3]Laboratory of Molecular Cell Dynamics, Faculty of Advanced Life Science, Hokkaido University, Kita-21 Nishi-11, Kita-ku, Sapporo, Hokkaido 001-0021, Japan

Abstract

Number and brightness (N&B) analysis is useful for monitoring the spatial distribution of the concentration and oligomeric state of fluorescently labeled proteins in cells. N&B analysis is based on the statistical analysis of fluorescence images by using the method of moments (MoM). Further, N&B analysis can determine the particle number and particle brightness, which indicate the concentration and oligomeric state, respectively. However, the statistical accuracy and precision are limited in actual experiments with fluorescent proteins, owing to low excitation and the limited number of images. In this study, we applied maximum likelihood (ML) estimation and maximum a posteriori (MAP) estimation coupled with the empirical Bayes (EB) method (referred to as EB–MAP). In EB–MAP, we constructed a simple prior distribution for a pixel to utilize the information of the surrounding pixels. To evaluate the accuracy and precision of our method, we conducted simulations and experiments and compared the results of MoM, ML, and EB–MAP. The results showed that MoM estimated the particle number with many outliers. The outliers hampered the visibility of the spatial distribution and cellular structure. In contrast, EB–MAP suppressed the number of outliers and improved the visibility notably. The precision of EB–MAP was better by an order of magnitude in terms of particle number and 1.5 times better in terms of particle brightness compared with those of MoM. The proposed method (EB–MAP–N&B) is applicable to studies on fluorescence imaging, and would aid in accurately recognizing changes in the concentration and oligomeric state in cells. Our results hold significant importance because quantifying the concentration and oligomeric state would contribute to the understanding of dynamic processes in molecular mechanism in cells.

Statement of Significance

Quantifying the concentration and oligomeric state of molecules would provide valuable information about molecular mechanisms; however, it is challenging to quantify them in cells. N&B analysis characterizes the concentration and oligomeric state of fluorescently labeled molecules by statistically analyzing fluorescence images. Although 30 years have passed since the reporting of this theory, only a few solutions have been reported to improve its accuracy and precision at a fundamental level. Therefore, we propose empirical Bayes–maximum a posteriori (EB–MAP) estimation, which utilizes the surrounding pixel information. We demonstrated the accuracy and precision of EB–MAP to be markedly better than those of the conventional method.

Introduction

Fluorescence imaging reveals the localization and distribution of fluorescently labeled molecules in cells. The concentration of molecules is strongly related to the progress of chemical reactions in cells, and the reactions regulate cellular functions. Thus, quantifying the concentration would yield valuable information about the regulations and the functions of cells. However, changes in the fluorescence intensity of images are caused by changes in the concentration and brightness of a single particle. Thus, with the exception of single molecule detection, it is challenging to quantify the concentration of fluorescent molecules from only the fluorescence images. Continuously observing the changes in fluorescence intensity allows for the deconstruction of the fluorescence intensity into two factors.

Fluorescence fluctuation spectroscopy (FFS) (1–3) is a general term for methods that analyze the temporal and spatial fluctuations in fluorescence intensity; it also provides useful information on factors such as concentration, oligomeric state, and rate of diffusion. Fluorescence correlation spectroscopy (FCS) (4) is a well-known method based on the statistical analysis of temporally correlated fluctuations caused by diffusing particles. The measurement type of this method is a single-spot measurement, typically achieved using confocal fluorescence microscopy. Fluorescent particles freely diffuse and pass through the confocal volume (i.e., measurement volume) created by microscopy. Microscopy records the fluctuation in fluorescence intensity over time, and the fluctuation is described as an autocorrelation function. Typically, the weighted least squares method determines the parameters of the autocorrelation function. However, with the exception of several reports (5, 6), FCS could obtain single-spot information.

Number and brightness (N&B) analysis (7) is another method based on the statistical analysis of temporally independent fluctuations in photon-counting images. In this method, images are typically obtained using confocal laser scanning microscopy. This microscopy method successively counts photons within a given sampling time while scanning and recording the counts as an image consisting of pixels. Iterative scanning produces a sequence of images, and the temporal fluctuation at each pixel position is analyzed based on the method of moments (MoM). Let us define an imaging duration as the period between a sampling and the next sampling at a pixel position. Under typical measurement conditions, the sampling time for a single pixel is less than several tens of microseconds, and the imaging duration is between hundreds of milliseconds to seconds for images of a sufficiently large size. This imaging duration is sufficient for fluorescent particles to pass through the confocal volume, and the temporal fluctuations become independent, unlike those in FCS because of the long imaging duration. In MoM, the first and second raw moments are estimated; moments are characteristic values of the probability distribution. The first moment is the sample average, and the second is an element constituting sample variance. The estimator consisting of the moments gives the particle number and particle brightness (7–10). The particle number reflects the concentration, whereas the particle brightness reflects the fluorescence intensity of a single particle. The fold change in particle brightness can be used to infer the oligomeric state. In the dimerization of two monomers into a dimer (Fig. 1), the fluorescence intensities of the monomers and the dimers are the same. In contrast, the numbers of particles are different, i.e., 2 and 1 for the monomers and the dimers, respectively. A dimer carries two fluorescent proteins; thus, the particle brightness of a dimer is twice that of a monomer.

FCS is a single-spot measurement, whereas N&B analysis is a two-dimensional imaging-based measurement. The N&B analysis determines the particle number and particle brightness at each pixel position, and reveals their distribution as an image. Thus, N&B analysis is advantageous for monitoring the wide spatial range in cells. However,

the conventional method estimates the particle number and particle brightness with low accuracy and precision in a practical experiment with fluorescent proteins. Theoretically, a measurement with high excitation and an analysis with a large number of images yield accurate and precise estimation; however, they cause photobleaching and have low time-resolution in an actual experiment. If photobleaching occurs, MoM underestimates the particle number and overestimates the particle brightness. Under undesired conditions, such as low excitation and small number of images, the particle number and particle brightness are sometimes estimated negatively, and outliers of particle number appear often. In this report, we consider the estimation of the particle number and particle brightness in the absence of photobleaching.

In this study, we evaluated the performance of three different approaches, namely, MoM estimation, maximum likelihood (ML) estimation, and maximum a posteriori (MAP) estimation coupled with the empirical Bayes (EB) method (hereinafter referred to as EB–MAP). Regarding MoM, Qian and Elson reported a basic theory for N&B analysis in 1990, and Digman et al. applied it to laser scanning microscopy in 2008. However, little research has been conducted on devising solutions to improve the accuracy and precision of N&B analysis at a fundamental level, although it has been 30 years since the introduction of this theory. Furthermore, the application of ML estimation and EB–MAP to N&B analysis has not been studied before. In the estimation using MoM, we adopted two-detector N&B (TD–N&B) analysis, which reduces the effect of afterpulse and dead time reported previously (11). The ML determines the parameters by maximizing the likelihood function. The MAP estimation is a Bayesian approach, and utilizes prior distribution in addition to the likelihood function. The advantages of ML and Bayesian approaches have been reported in several studies. Strey investigated the least squares method and ML for the autocorrelated time trace originating from the Ornstein–Uhlenbeck process (12). He reported that using the least squares method in FCS causes systematic deviation from the true parameters. Jazani et al. reported such a deviation in FCS using Bayesian non-parametrics (13). Regarding the fluorescence lifetime measurement, Santra et al. investigated the least squares method, ML, and the related methods, and reported robustness of ML (14, 15). In the N&B analysis, a simple assumption (detailed later, before Eq. 3) enables the description of the probability distribution of photon counts based on Neyman type A distribution. Shenton evaluated the asymptotic efficiency of an MoM estimator (16), and Shenton and Bowman investigated the bias and variance of MoM and ML with a sample size of 100 (17). These reports suggested that the estimations of ML are more precise than those of MoM. However, ML sometimes estimates the particle number and particle brightness as infinity and 0, respectively, although their parameter space is limited on the intervals over 0 and below infinity; these estimates are known as boundary estimates (18, 19).

To avoid such parameters, we applied MAP estimation. The prior distribution acts as a regularization term and prevents the boundary estimates. We assumed that the distribution of the particle number at a pixel and the surrounding pixels follows lognormal distribution. Then, we applied the EB method to determine the parameters of the distribution. Finally, we demonstrated the feasibility of our methods by simulations and experiments on an enhanced green fluorescent protein (EGFP) solution and the cells expressing EGFP tandem-oligomers.

THEORY

Photon-counting model

Single detector

We constructed a double-detector system for single-color imaging by coupling a half mirror. In our single-detector system, the saturation of the photon count in the avalanche photodiode is severe if the fluorescence intensity is higher than 500 kHz. To extend the applicability of our method, we included the half mirror and reduced the fluorescence intensity of the detector. First, we describe a theory for photon counting by a single detector, and then extend the theory to double detectors.

A semiclassical description of photon counting was made by Mandel (20). Here, we make assumptions based on the theory of photon counting histogram (PCH) (21). Let $I_t(t)$ be the instantaneous light intensity of a detector at time t, and T be the sampling time. The light intensity at a sampling time is given by the integral from t to $t + T$ of $I_t(t)$. Here, we assume that the sampling time is sufficiently short compared with the residence time of the diffusing particles in the confocal volume. This assumption indicates that the number of particles does not change during the sampling time, and thus enables to track the number of particles at the moment of sampling. Under this assumption, the light intensity during the sampling time is given by $I_t T$, and the probability distribution for observing W photons during sampling by a single detector is given by rewriting Mandel's formula (21, 22):

$$P(W|\eta) = \int_0^\infty \mathrm{Poi}(W|\eta I_0) P(I_0) \mathrm{d} I_0, \tag{1}$$

where η denotes the detection efficiency of the detector; I_0 is the integrated light intensity ($I_0 = I_t T$); $P(I_0)$ is the probability distribution for I_0; $\mathrm{Poi}(W|\eta I_0)$ is a Poisson distribution given as follows:

$$\mathrm{Poi}(W|\eta I_0) = \frac{(\eta I_0)^W}{W!} \exp(-\eta I_0). \tag{2}$$

We simply assume that the intensity fluctuation depends only on the changes in the number of particles, and the fluctuation follows Poisson distribution. The probability distribution for observing W photons is given by Neyman type A distribution as follows:

$$\mathrm{Ney}(W|\nu, \varepsilon) = \sum_{Z=0}^\infty \mathrm{Poi}(W|\varepsilon Z) \mathrm{Poi}(Z|\nu), \tag{3}$$

where ν denotes the particle number ($0 < \nu$), a parameter of the Poisson distribution characterizing the fluctuation in the instantaneous number of particles in the confocal volume; Z is a hidden variable and a realized outcome of the Poisson distribution; ε denotes particle brightness ($0 < \varepsilon$), an average photon count from a single particle within a sampling time; and ε/T represents the particle brightness in Hz. Calculating the probabilities using Eq. 3 is difficult because it contains an infinite series; however, the following recursive formula is available (23, 24):

$$\text{Ney}(W|v,\varepsilon) = \begin{cases} \exp[v\{\exp(-\varepsilon)-1\}], & (W = 0), \\ \dfrac{1}{W}v\varepsilon\exp(-\varepsilon)\displaystyle\sum_{l=0}^{W-1}\dfrac{\varepsilon^{W-l-1}}{(W-l-1)!}\text{Ney}(l|v,\varepsilon), & (W \geq 1). \end{cases} \tag{4}$$

Double detectors

We extend the equations obtained above to a double-detector system. The light intensity is separated by a half mirror and detected by two photon detectors. Let I_1 and I_2 be integrated light intensities in detector 1 and 2, respectively. The probability distribution for observing X and Y photons at detector 1 and 2, respectively, is given as follows (22):

$$P(X,Y|\eta_1,\eta_2) = \int_0^\infty \int_0^\infty \text{Poi}(X|\eta_1 I_1)\text{Poi}(Y|\eta_2 I_2)P(I_1,I_2)\,dI_1\,dI_2, \tag{5}$$

where η_1 and η_2 denote the detection efficiency of detector 1 and 2, respectively. Under the same assumptions as those for Eq. 3, the probability distribution for observing X and Y photons is given by

$$\begin{aligned} P(X,Y|v,\varepsilon,p) &= \sum_{Z=0}^\infty \text{Poi}(X|\varepsilon p Z)\text{Poi}(Y|\varepsilon(1-p)Z)\text{Poi}(Z|v) \\ &= \text{Bin}(X,Y|p)\text{Ney}(W|v,\varepsilon), \end{aligned} \tag{6}$$

where p represents a fraction of light intensity reaching detector 1, W is equal to $X + Y$, and $\text{Bin}(X,Y|p)$ is a binomial distribution given by

$$\text{Bin}(X,Y|p) = \frac{(X+Y)!}{X!\,Y!}p^X(1-p)^Y. \tag{7}$$

The recursive formula similar to Eq. 4 is given by (see Supporting Material for derivation)

$$P(X,Y|v,\varepsilon,p) = \begin{cases} \exp[v(\exp[-\varepsilon]-1)], & (X=0,Y=0), \\ \dfrac{1}{Y}v\varepsilon(1-p)\exp[-\varepsilon]\displaystyle\sum_{m=0}^{Y-1}\dfrac{\{(1-p)\varepsilon\}^{Y-m-1}}{(Y-m-1)!}P(0,m|v,\varepsilon,p), & (X=0,Y\geq 1), \\ \dfrac{1}{X}v\varepsilon p\exp[-\varepsilon]\displaystyle\sum_{m=0}^{Y}\dfrac{\{(1-p)\varepsilon\}^{Y-m}}{(Y-m)!}\sum_{l=0}^{X-1}\dfrac{(p\varepsilon)^{X-l-1}}{(X-l-1)!}P(l,m|v,\varepsilon,p), & (X\geq 1,Y\geq 0). \end{cases} \tag{8}$$

Single detector affected by dead time

Dead time is a non-ideal property of a photon detector that causes loss of photon count. Dead time is a time period after photon detection during which detectors cannot detect any photons. Underestimation of particle brightness without correction for dead time has been reported (11, 25). Let τ be the dead time, and $\delta = \tau/T$. The probability distribution for observing W photons on a dead-time-affected detector is given as follows for $W < 1/\delta$ (see

Supporting Material for derivation):

$$P(W|v, \varepsilon, \delta) = \sum_{m=0}^{\infty} A_m(W, \delta) \text{Ney}(W + m|v, \varepsilon),$$

(9)

where the function $A_m(W, \delta)$ is given by

$$A_m(W, \delta) = \binom{W + m}{W} \sum_{k=m}^{W+m} (-1)^{k-m} \binom{W}{k - m} \delta^k \left[\left(1 - \frac{m}{k}\right)(W - 1)^k + \frac{m}{k} W^k \right].$$

(10)

Double detectors affected by dead time

For a double-detector system, let τ_1 and τ_2 be the dead time for detectors 1 and 2, respectively, and let us define $\delta_1 = \tau_1/T$ and $\delta_2 = \tau_2/T$. The joint probability distribution for observing X and Y photons on a dead-time-affected detector is given as follows for $X < 1/\delta_1$ and $Y < 1/\delta_2$ (see Supporting Material for derivation):

$$P(X, Y|v, \varepsilon, p, \delta_1, \delta_2) = \sum_{m=0}^{\infty} \sum_{h=0}^{m} A_h(X, \delta_1) A_{m-h}(Y, \delta_2) P(X + h, Y + m - h|v, \varepsilon, p).$$

(11)

In this study, we assumed that higher terms of the infinite series, such as $3 \leq m$, are negligible.

Maximum likelihood estimation

Double-detector model

The ML determines parameters by maximizing a likelihood function. We assume independent I time observations. In the N&B analysis, independent observations are realized if the imaging duration is sufficiently longer than the residence time of the fluorescent particles in the confocal volume. The likelihood function is given as follows, with $\boldsymbol{x} = (x_1, x_2, \dots, x_I)$ and $\boldsymbol{y} = (y_1, y_2, \dots, y_I)$:

$$\mathcal{L}(\boldsymbol{x}, \boldsymbol{y}|v, \varepsilon, p) = \prod_{i=1}^{I} P(x_i, y_i|v, \varepsilon, p).$$

(12)

We numerically estimate the maximum point on the natural logarithm of the likelihood function by using the Newton–Raphson method. This is an iterative method and requires the first and second derivatives of the log-likelihood function. The first derivatives with respect to the parameters are given by,

$$\frac{\partial \log \mathcal{L}}{\partial v}(\boldsymbol{x}, \boldsymbol{y}|v, \varepsilon, p) = -I + \frac{1}{v\varepsilon} S_1(\boldsymbol{x} + \boldsymbol{y}, v, \varepsilon),$$

(13)

$$\frac{\partial \log \mathcal{L}}{\partial \varepsilon}(\boldsymbol{x}, \boldsymbol{y} | v, \varepsilon, p) = \frac{1}{\varepsilon} S_0(\boldsymbol{x} + \boldsymbol{y}) - \frac{1}{\varepsilon} S_1(\boldsymbol{x} + \boldsymbol{y}, v, \varepsilon), \tag{14}$$

$$\frac{\partial \log \mathcal{L}}{\partial p}(\boldsymbol{x}, \boldsymbol{y} | v, \varepsilon, p) = \frac{1}{p} S_0(\boldsymbol{x}) - \frac{1}{1 - p} S_0(\boldsymbol{y}), \tag{15}$$

where

$$S_0(\boldsymbol{w}) := \sum_{i=1}^{I} w_i, \tag{16}$$

$$S_1(\boldsymbol{w}, v, \varepsilon) := \sum_{i=1}^{I} \frac{(w_i + 1)\mathrm{Ney}(w_i + 1 | v, \varepsilon)}{\mathrm{Ney}(w_i | v, \varepsilon)}, \tag{17}$$

$\boldsymbol{w} = (w_1, w_2, \ldots, w_I)$, and $w_i = x_i + y_i$ $(i = 1, 2, \ldots, I)$. Setting the first derivatives to zero gives

$$v\varepsilon = \frac{1}{I} \sum_{i=1}^{I} (x_i + y_i), \tag{18}$$

$$\hat{p} = \frac{\sum_{i=1}^{I} x_i}{\sum_{i=1}^{I} (x_i + y_i)}. \tag{19}$$

Substituting $\varepsilon = \bar{w}/v$ $(\bar{w} = \frac{1}{I}\sum_{i=1}^{I} x_i + y_i)$ into the probability distribution and the log-likelihood function gives a univariate likelihood function. The first and second derivatives with respect to v are given by,

$$\frac{\partial \log \mathcal{L}}{\partial v}\left(\boldsymbol{x}, \boldsymbol{y} \middle| v, \frac{\bar{w}}{v}, p\right) = -I - \frac{I\bar{w}}{v} + \left(\frac{1}{v} + \frac{1}{\bar{w}}\right) S_1\left(\boldsymbol{x} + \boldsymbol{y}, v, \frac{\bar{w}}{v}\right), \tag{20}$$

$$\frac{\partial^2 \log \mathcal{L}}{\partial v^2}\left(\boldsymbol{x}, \boldsymbol{y} \middle| v, \frac{\bar{w}}{v}, p\right)$$
$$= \frac{I\bar{w}}{v^2} - \frac{1}{v}\left(\frac{2}{v} + \frac{1}{\bar{w}}\right) S_1\left(\boldsymbol{x} + \boldsymbol{y}, v, \frac{\bar{w}}{v}\right) + \left(\frac{1}{v} + \frac{1}{\bar{w}}\right)^2 S_2\left(\boldsymbol{x} + \boldsymbol{y}, v, \frac{\bar{w}}{v}\right) \tag{21}$$
$$- \left(\frac{1}{v} + \frac{1}{\bar{w}}\right)^2 S_3\left(\boldsymbol{x} + \boldsymbol{y}, v, \frac{\bar{w}}{v}\right),$$

where

$$S_2(\boldsymbol{w}, v, \varepsilon) := \sum_{i=1}^{I} \frac{(w_i + 1)(w_i + 2)\mathrm{Ney}(w_i + 2 | v, \varepsilon)}{\mathrm{Ney}(w_i | v, \varepsilon)}, \tag{22}$$

$$S_3(\boldsymbol{w}, v, \varepsilon) := \sum_{i=1}^{I} \left\{ \frac{(w_i + 1)\mathrm{Ney}(w_i + 1 | v, \varepsilon)}{\mathrm{Ney}(w_i | v, \varepsilon)} \right\}^2. \tag{23}$$

For the initial value of $v^{(0)}$, the k-th iteration process of the Newton–Raphson method ($k = 0,1,2,...$) is given by,

$$v^{(k+1)} = v^{(k)} - \frac{\frac{\partial \log \mathcal{L}}{\partial v}\left(x, y\middle|v, \frac{\overline{w}}{v}, p\right)}{\frac{\partial^2 \log \mathcal{L}}{\partial v^2}\left(x, y\middle|v, \frac{\overline{w}}{v}, p\right)}. \tag{24}$$

Dead-time-affected double-detector model

The likelihood function for a dead-time-affected photon count is given by,

$$\mathcal{L}(x, y|v, \varepsilon, p, \delta_1, \delta_2) = \prod_{i=1}^{I} P(x_i, y_i|v, \varepsilon, p, \delta_1, \delta_2). \tag{25}$$

In the dead-time-affected model, the relationship between v and ε, similar to Eq. 18, was not obtained; thus, we use the Newton–Raphson method for two variables to find the maximum of the likelihood function. The first and second derivatives of the log-likelihood function are calculated from the probability distribution for the dead-time-affected photon count and the first and second derivatives of this probability distribution. The first and second derivatives are obtained by taking the derivative of Eq. 11. We assumed a constant dead time of 50 ns ($\delta_1 = \delta_2 = 7.82 \times 10^{-3}$). The first and second derivatives of the probability distribution for an ideal photon count are given by,

$$\frac{\partial P}{\partial v}(X, Y|v, \varepsilon, p) = -P(X, Y|v, \varepsilon, p) + \frac{X+1}{v\varepsilon p}P(X+1, Y|v, \varepsilon, p), \tag{26}$$

$$\frac{\partial P}{\partial \varepsilon}(X, Y|v, \varepsilon, p) = \frac{X+Y}{\varepsilon}P(X, Y|v, \varepsilon, p) - \frac{X+1}{\varepsilon p}P(X+1, Y|v, \varepsilon, p), \tag{27}$$

$$\frac{\partial^2 P}{\partial v^2}(X, Y|v, \varepsilon, p)$$

$$= P(X, Y|v, \varepsilon, p) - \frac{(2v+1)(X+1)}{v^2 \varepsilon p}P(X+1, Y|v, \varepsilon, p) \tag{28}$$

$$+ \frac{(X+1)(X+2)}{v^2 \varepsilon^2 p^2}P(X+2, Y|v, \varepsilon, p),$$

$$\frac{\partial^2 P}{\partial v \partial \varepsilon}(X, Y|v, \varepsilon, p)$$

$$= -\frac{X+Y}{\varepsilon}P(X, Y|v, \varepsilon, p) + \frac{(X+Y+v\varepsilon)(X+1)}{v\varepsilon^2 p}P(X+1, Y|v, \varepsilon, p) \tag{29}$$

$$- \frac{(X+1)(X+2)}{v\varepsilon^2 p^2}P(X+2, Y|v, \varepsilon, p),$$

$$\frac{\partial^2 P}{\partial \varepsilon^2}(X,Y|\nu,\varepsilon,p)$$

$$= \frac{(X+Y)(X+Y-1)}{\varepsilon^2}P(X,Y|\nu,\varepsilon,p) - \frac{2(X+Y)(X+1)}{\varepsilon^2 p}P(X+1,Y|\nu,\varepsilon,p) \qquad (30)$$

$$+ \frac{(X+1)(X+2)}{\varepsilon^2 p^2}P(X+2,Y|\nu,\varepsilon,p).$$

For the initial values of $\nu^{(0)}$ and $\varepsilon^{(0)}$, the k-th iteration process of the Newton–Raphson method ($k = 1,2,3,...$) is given by,

$$\begin{pmatrix} \nu^{(k+1)} \\ \varepsilon^{(k+1)} \end{pmatrix} = \begin{pmatrix} \nu^{(k)} \\ \varepsilon^{(k)} \end{pmatrix} - \begin{pmatrix} \dfrac{\partial^2 \log L}{\partial \nu^2} & \dfrac{\partial^2 \log L}{\partial \nu \partial \varepsilon} \\ \dfrac{\partial^2 \log L}{\partial \nu \partial \varepsilon} & \dfrac{\partial^2 \log L}{\partial \varepsilon^2} \end{pmatrix}^{-1} \begin{pmatrix} \dfrac{\partial \log L}{\partial \nu} \\ \dfrac{\partial \log L}{\partial \varepsilon} \end{pmatrix}, \qquad (31)$$

where $\log \mathcal{L}$ is the abbreviated form of $\log \mathcal{L}(\boldsymbol{x},\boldsymbol{y}|\nu,\varepsilon,p,\delta_1,\delta_2)$.

Maximum a posteriori estimation

In ML, the estimates are sometimes on the boundary of the parameter space, which are known as boundary estimates (18, 19). In our N&B analysis, although the parameter space of ν and ε is $0 < \nu < \infty$ and $0 < \varepsilon < \infty$, respectively, the maximum point of the log-likelihood is sometimes given by ν of infinity and ε of 0 (see Fig. S3.3 in Supporting Material). Some studies have reported that boundary estimates are obtained via analyses using a statistical model that contains hidden variables, and appear on a small sample size (18). In fact, N&B analysis has a hidden variable Z for the number of particles at the moment of a sampling. The boundary estimates appeared well in an analysis with a small frame number or low particle brightness (see Fig. S3.1 in Supporting Material). To avoid the estimates, we applied MAP estimation. A MAP estimate is given by maximizing the product of the likelihood function and prior distribution. The prior distribution is a probability distribution, which characterizes the uncertainty of the parameters before observations. The prior distribution prevents the estimates from moving to the boundary.

In this study, we assumed lognormal distribution as the prior distribution to represent the similarity in particle number between a pixel and the surrounding eight pixels. For N&B analysis, the assumption of similarity would be realistic, because of two reasons. (a) Diffraction limit: diffraction prevents a microscope from imaging the light emitted from a point light source. Even if the particle number changes sharply between a pixel and the surrounding eight pixels, the change would be alleviated. (b) Overlap of confocal volume during sampling: to maintain the lateral resolution, a pixel size smaller than the resolution is recommended. Confocal laser scanning microscopy scans the pixel size within a sampling time. During scanning, the illuminated area overlaps between the adjacent pixels if the confocal volume has a radius as large as the pixel size. We simply consider a fraction of the overlap in the x–y plane. In our measurement, we used an excitation wavelength of 488 nm and a numerical aperture of 1.2; further, we theoretically calculated the radius of the Airy disk (lateral resolution) as 248 nm. We set a pixel size of 146 nm and estimated the radius of the confocal volume as 214 nm by using FCS (see Materials and Methods in Supporting Material). The overlap fraction of the illuminated area can be calculated by $\pi r^2/(\pi r^2 + 2sr)$, where r is the radius of the confocal volume and s is the pixel size (see Supporting Material for derivation). In our

measurement, this fraction is 0.697, suggesting that the illuminated area does not change markedly in the adjacent pixels. To determine the parameters of the lognormal distribution, we applied the EB method to a pixel by using the surrounding eight pixels. The EB method is described later.

Double-detector model

We assumed that the prior distributions of the particle number ν and particle brightness ε are independent, and are given by lognormal and uniform distributions from 0 to ∞, respectively. The joint posterior distribution is given by

$$P(\nu, \varepsilon | \boldsymbol{x}, \boldsymbol{y}, \hat{p}, \hat{\mu}, \hat{\sigma}) \propto \mathcal{L}(\boldsymbol{x}, \boldsymbol{y} | \nu, \varepsilon, \hat{p}) \mathrm{LN}(\nu | \hat{\mu}, \hat{\sigma}) \mathrm{Uni}(\varepsilon), \tag{32}$$

where $\hat{p}$ is an estimate for p. We assumed that p can be approximated as a constant independent of the pixel position and measurements, and can be estimated prior to the measurements by using Eq. 19 ($\hat{p} = 0.5665$). The same assumption is used in the following. Further, $\hat{\mu}$ and $\hat{\sigma}$ are estimates given by the EB method; LN and Uni represent the lognormal and uniform distributions, respectively. We estimated the maximum of the joint posterior distribution using the Newton–Raphson method as before. Taking the logarithm of both sides on Eq. 32 and the derivative of the log-posterior distribution gives the equations required for the Newton–Raphson method. The first and second derivatives of $\log \mathcal{L}(\boldsymbol{x}, \boldsymbol{y} | \nu, \varepsilon, \hat{p})$ and $\log \mathrm{LN}(\nu | \hat{\mu}, \hat{\sigma})$ are given by Eq. 13 and 14, and

$$\frac{\partial^2 \log \mathcal{L}}{\partial \nu^2}(\boldsymbol{x}, \boldsymbol{y} | \nu, \varepsilon, \hat{p}) = -\frac{1}{\nu^2 \varepsilon} S_1(\boldsymbol{x} + \boldsymbol{y}, \nu, \varepsilon) + \frac{1}{\nu^2 \varepsilon^2} S_2(\boldsymbol{x} + \boldsymbol{y}, \nu, \varepsilon) - \frac{1}{\nu^2 \varepsilon^2} S_3(\boldsymbol{x} + \boldsymbol{y}, \nu, \varepsilon), \tag{33}$$

$$\frac{\partial^2 \log \mathcal{L}}{\partial \nu \partial \varepsilon}(\boldsymbol{x}, \boldsymbol{y} | \nu, \varepsilon, \hat{p}) = -\frac{1}{\nu \varepsilon^2} S_2(\boldsymbol{x} + \boldsymbol{y}, \nu, \varepsilon) + \frac{1}{\nu \varepsilon^2} S_3(\boldsymbol{x} + \boldsymbol{y}, \nu, \varepsilon), \tag{34}$$

$$\frac{\partial^2 \log \mathcal{L}}{\partial \varepsilon^2}(\boldsymbol{x}, \boldsymbol{y} | \nu, \varepsilon, \hat{p}) = -\frac{1}{\varepsilon^2} S_0(\boldsymbol{x} + \boldsymbol{y}) + \frac{1}{\varepsilon^2} S_2(\boldsymbol{x} + \boldsymbol{y}, \nu, \varepsilon) - \frac{1}{\varepsilon^2} S_3(\boldsymbol{x} + \boldsymbol{y}, \nu, \varepsilon), \tag{35}$$

$$\frac{\partial \log \mathrm{LN}}{\partial \nu}(\nu | \hat{\mu}, \hat{\sigma}) = -\frac{1}{\nu} - \frac{\log \nu - \hat{\mu}}{\hat{\sigma}^2 \nu}, \tag{36}$$

$$\frac{\partial^2 \log \mathrm{LN}}{\partial \nu^2}(\nu | \hat{\mu}, \hat{\sigma}) = \frac{1}{\nu^2} + \frac{\log \nu - \hat{\mu} - 1}{\hat{\sigma}^2 \nu^2}. \tag{37}$$

For the initial values of $\nu^{(0)}$ and $\varepsilon^{(0)}$, the k-th iteration process of the Newton–Raphson method ($k = 1,2,3, \dots$) is given by Eq. 31 by replacing $\log \mathcal{L}$ with $\log P(\nu, \varepsilon | \boldsymbol{x}, \boldsymbol{y}, \hat{p}, \hat{\mu}, \hat{\sigma})$.

Dead-time-affected double-detector model

The joint posterior distribution is given by

$$P(\nu, \varepsilon | \boldsymbol{x}, \boldsymbol{y}, \hat{p}, \delta_1, \delta_2, \hat{\mu}, \hat{\sigma}) \propto \mathcal{L}(\boldsymbol{x}, \boldsymbol{y} | \nu, \varepsilon, \hat{p}, \delta_1, \delta_2) \, \mathrm{LN}(\nu | \hat{\mu}, \hat{\sigma}) \mathrm{Uni}(\varepsilon). \tag{38}$$

To find the maximum of the posterior distribution, we used the Newton–Raphson method for two variables as done previously. The first and second derivatives of the log-posterior distribution are given by those of the log-likelihood and log-prior distribution, which are given by Eq. 25, 36, and 37. The iteration process of the Newton–Raphson method is given by Eq. 31 by replacing $\log \mathcal{L}$ with $\log P(\nu, \varepsilon | \boldsymbol{x}, \boldsymbol{y}, \hat{p}, \delta_1, \delta_2, \hat{\mu}, \hat{\sigma})$.

Empirical Bayes Method

Lognormal prior model

As mentioned above, we assumed that the particle number distributions of a pixel (center pixel) and the surrounding eight pixels are given by identical lognormal distributions. The parameter of the lognormal distribution is a hyperparameter, and we estimated the hyperparameters μ and σ for predicting the center pixel by using the surrounding eight pixels. In this study, we estimated the hyperparameters using the EB method (26, 27); this method determines the hyperparameters by maximizing the marginal likelihood. To find the maximum point, we used the expectation maximization (EM) algorithm (26, 27). We simply write the joint posterior distribution on the surrounding pixels with $v_{1:J} = (v_1, v_2 \ldots, v_J)$ and $\varepsilon_{1:J} = (\varepsilon_1, \varepsilon_2 \ldots, \varepsilon_J)$ as follows:

$$P\big(v_{1:J}, \varepsilon_{1:J} \,|\, x_{1:J}, y_{1:J}, \hat{p}, \mu, \sigma\big) = \frac{1}{\mathcal{M}} \prod_{j=1}^{J} \big[\mathcal{L}\big(x_j, y_j \,|\, v_j, \varepsilon_j, \hat{p}\big) \text{LN}\big(v_j \,|\, \mu, \sigma\big) \text{Uni}\big(\varepsilon_j\big)\big], \tag{39}$$

where the subscript j represents the addresses between the surrounding pixels, subscript $1:J$ represents the vector of the addresses (in this study, $J = 8$). The photon count observations at each pixel are assumed to be conditionally independent given μ and σ. For MoM and ML, photon count observations at each pixel are assumed to be independent. $\mathcal{M}$ is the marginal likelihood given by

$$\mathcal{M}\big(x_{1:J}, y_{1:J} \,|\, \hat{p}, \mu, \sigma\big) = \int_0^\infty \int_0^\infty \prod_{j=1}^{J} \big[\mathcal{L}\big(x_j, y_j \,|\, v_j, \varepsilon_j, \hat{p}\big) \text{LN}\big(v_j \,|\, \mu, \sigma\big) \text{Uni}\big(\varepsilon_j\big)\big] \, dv_{1:J} \, d\varepsilon_{1:J}$$

$$= \prod_{j=1}^{J} \bigg[\int_0^\infty \int_0^\infty \mathcal{L}\big(x_j, y_j \,|\, v_j, \varepsilon_j, \hat{p}\big) \text{LN}\big(v_j \,|\, \mu, \sigma\big) \text{Uni}\big(\varepsilon_j\big) dv_j \, d\varepsilon_j\bigg]. \tag{40}$$

The EM algorithm is an iterative method to find the maximum, which is given by maximizing the following function $Q(\mu, \sigma, \mu_{\text{old}}, \sigma_{\text{old}})$ (see Supporting Material for derivation):

$$Q(\mu, \sigma, \mu_{\text{old}}, \sigma_{\text{old}}) = \sum_{j=1}^{J} \int_0^\infty \int_0^\infty P\big(v_j, \varepsilon_j \,|\, x_j, y_j, \hat{p}, \mu_{\text{old}}, \sigma_{\text{old}}\big) \log \text{LN}\big(v_j \,|\, \mu, \sigma\big) \, dv_j \, d\varepsilon_j. \tag{41}$$

The algorithm consists of an E step and an M step. The E step is a calculation step of expectations with the fixed hyperparameters μ_{old} and σ_{old}. The M step is a maximization step of $Q(\mu, \sigma, \mu_{\text{old}}, \sigma_{\text{old}})$ by changing the hyperparameters μ and σ. The first derivative of $Q(\mu, \sigma, \mu_{\text{old}}, \sigma_{\text{old}})$ is given by,

$$\frac{\partial Q}{\partial \mu}(\mu, \sigma, \mu_{\text{old}}, \sigma_{\text{old}}) = \frac{1}{\sigma^2} \sum_{j=1}^{J} \big[\mathbb{E}_{v_j \varepsilon_j}[\log v_j] - \mu\big], \tag{42}$$

$$\frac{\partial Q}{\partial \sigma}(\mu, \sigma, \mu_{\text{old}}, \sigma_{\text{old}}) = \sum_{j=1}^{J} \left[-\frac{1}{\sigma} + \frac{\mathbb{E}_{\nu_j \varepsilon_j}\left[(\log \nu_j - \mu)^2 \right]}{\sigma^3} \right], \tag{43}$$

where $\mathbb{E}_{\nu_j \varepsilon_j}[\ ]$ denotes an expectation with posterior distribution $P(\nu_j, \varepsilon_j, |\mathbf{x}_j, \mathbf{y}_j, \hat{p}, \mu_{\text{old}}, \sigma_{\text{old}})$. Setting the first derivatives to zero gives

$$\mu_{\text{new}} = \frac{1}{J} \sum_{j=1}^{J} \mathbb{E}_{\nu_j \varepsilon_j}\left[\log \nu_j \right], \tag{44}$$

$$\sigma_{\text{new}} = \left(\frac{1}{J} \sum_{j=1}^{J} \mathbb{E}_{\nu_j \varepsilon_j}\left[(\log \nu_j)^2 \right] - \mu_{\text{new}}^2 \right)^{\frac{1}{2}}. \tag{45}$$

In this model, $\mathbb{E}_{\nu_j \varepsilon_j}[\log \nu_j]$ and $\mathbb{E}_{\nu_j \varepsilon_j}\left[(\log \nu_j)^2 \right]$ are calculated in the E step, and μ_{new} and σ_{new} are estimated in the M step. The estimated μ_{new} and σ_{new} are used as μ_{old} and σ_{old}, respectively, in the following E step. The iteration of the E step and the M step continues until convergence.

Lognormal prior with gamma hyperprior model

In the previously described lognormal prior model, the EB method gives the estimates, and the estimates can be substituted for lognormal distribution $\text{LN}(\nu|\hat{\mu}, \hat{\sigma})$. The distribution enables the prediction of particle number in a pixel. However, the precision of the estimates is insufficiently high; thus, the prediction sometimes fails (see Fig S1.1 in Supporting Material). The low precision could be attributed to the small number of grouped pixels; especially, a low $\hat{\sigma}$ reduces the variance of the distribution, and the prediction fails to represent the variation in the particle number of grouped pixels. To avoid this problem, Chung et al. proposed to use gamma distribution as a hyperprior (28). A hyperprior is a prior distribution for a hyperparameter, which acts as a penalty against a low $\hat{\sigma}$. A gamma hyperprior for σ is given by

$$\text{Gam}(\sigma|\alpha, \beta) = \frac{\beta^\alpha}{\Gamma(\alpha)} \sigma^{\alpha-1} \exp(-\beta\sigma), \tag{46}$$

where α and β are parameters taking a positive value ($0 < \alpha$, $0 < \beta$), $\Gamma(\alpha)$ is a gamma function, and $\Gamma(\alpha) = \int_0^\infty u^{\alpha-1} \exp(-u)\, du$. Chung et al. recommended to use $\alpha = 2$ and $\beta \to 0$ by default. In this study, we used $\alpha = J + 1$ and $\beta = 0.01J$ (we assumed $J = 8$; thus, $\alpha = 9$ and $\beta = 0.08$). We choose a pair of α and β to simplify the calculation in the M step and construct the gamma distribution with a mode of 100. With this choice, the 25th and 75th percentiles of the gamma distribution are $Q_{25} = 85.5$ and $Q_{75} = 135.0$, respectively. The gamma distribution works to positively increase $\hat{\sigma}$ and prevents the prediction from failing. Simply considering the default amount of particle number variation whose σ of 100 is given, the 25th and 75th percentiles for ν are $Q_{25} = 5.10 \times 10^{-30} \exp(\mu)$ and $Q_{75} = 1.96 \times 10^{29} \exp(\mu)$, respectively. The median of the distribution is given by $\exp(\mu)$. Although the percentiles depend on μ, the Q_{25}–Q_{75} interval would be regarded as sufficiently wide. An

actual experimental range of the particle number in an N&B analysis would be $10^{-3} < \nu < 10^3$. With a small particle number, the fluorescence background and autofluorescence are not negligible. In contrast, with a large particle number, the fluorescence intensity increases, and the photon count saturation of the detectors is not negligible. The joint posterior distribution is given by

$$P\left(\nu_{1:J}, \varepsilon_{1:J} | \boldsymbol{x}_{1:J}, \boldsymbol{y}_{1:J}, \hat{p}, \mu, \sigma, \alpha, \beta\right) = \frac{1}{\mathcal{M}} \prod_{j=1}^{J} \left[\mathcal{L}\left(\boldsymbol{x}_j, \boldsymbol{y}_j | \nu_j, \varepsilon_j, \hat{p}\right) \mathrm{LN}\left(\nu_j | \mu, \sigma\right) \mathrm{Uni}\left(\varepsilon_j\right)\right] \mathrm{Gam}(\sigma | \alpha, \beta), \quad (47)$$

where

$$\mathcal{M}\left(\boldsymbol{x}_{1:J}, \boldsymbol{y}_{1:J} | \hat{p}, \mu, \sigma, \alpha, \beta\right) = \prod_{j=1}^{J} \left[\int_0^\infty \int_0^\infty \mathcal{L}\left(\boldsymbol{x}_j, \boldsymbol{y}_j | \nu_j, \varepsilon_j, \hat{p}\right) \mathrm{LN}\left(\nu_j | \mu, \sigma\right) \mathrm{Uni}\left(\varepsilon_j\right) \mathrm{d}\nu_j \, \mathrm{d}\varepsilon_j\right] \mathrm{Gam}(\sigma | \alpha, \beta). \quad (48)$$

$\mathcal{Q}$ is given by (see Supporting Material for derivation),

$$\mathcal{Q}(\mu, \sigma, \mu_{\mathrm{old}}, \sigma_{\mathrm{old}})$$
$$= \sum_{j=1}^{J} \int_0^\infty \int_0^\infty P\left(\nu_j, \varepsilon_j, | \boldsymbol{x}_j, \boldsymbol{y}_j, \hat{p}, \mu_{\mathrm{old}}, \sigma_{\mathrm{old}}, \alpha, \beta\right) \log \mathrm{LN}\left(\nu_j | \mu, \sigma\right) \mathrm{d}\nu_j \, \mathrm{d}\varepsilon_j \quad (49)$$
$$+ \log \mathrm{Gam}(\sigma | \alpha, \beta).$$

The first derivatives are given by

$$\frac{\partial \mathcal{Q}}{\partial \mu}(\mu, \sigma, \mu_{\mathrm{old}}, \sigma_{\mathrm{old}}) = \frac{1}{\sigma^2} \sum_{j=1}^{J} \left[\mathbb{E}_{\nu_j \varepsilon_j}[\log \nu_j] - \mu\right], \quad (50)$$

$$\frac{\partial \mathcal{Q}}{\partial \sigma}(\mu, \sigma, \mu_{\mathrm{old}}, \sigma_{\mathrm{old}}) = \sum_{j=1}^{J} \left[-\frac{1}{\sigma} + \frac{\mathbb{E}_{\nu_j \varepsilon_j}\left[(\log \nu_j - \mu)^2\right]}{\sigma^3}\right] + \frac{\alpha - 1}{\sigma} - \beta. \quad (51)$$

Setting the first derivatives to zero and substituting $\alpha = J + 1$ gives

$$\mu_{\mathrm{new}} = \frac{1}{J} \sum_{j=1}^{J} \mathbb{E}_{\nu_j \varepsilon_j}[\log \nu_j], \quad (52)$$

$$\sigma_{\mathrm{new}} = \left[\frac{J}{\beta}\left\{\frac{1}{J}\sum_{j=1}^{J} \mathbb{E}_{\nu_j \varepsilon_j}\left[(\log \nu_j)^2\right] - \mu_{\mathrm{new}}^2\right\}\right]^{\frac{1}{3}}. \quad (53)$$

The model for a dead-time-affected detector is given by replacing $\mathcal{L}(x_j, y_j | \nu_j, \varepsilon_j, \hat{p})$ in Eq. 48 with $\mathcal{L}(x_j, y_j | \nu_j, \varepsilon_j, \hat{p}, \delta_1, \delta_2)$, and by replacing posterior distribution on the expectation.

RESULTS

Comparison of different concentrations by simulation

To determine if the ML and EB–MAP methods produce estimates accurately and precisely, we simulated images imitating measurements with different concentrations. Fig. 2A–F show the variation in estimates given by MoM (Fig. 2A and 2D), ML (Fig. 2B and 2E), and EB–MAP (Fig. 2C and 2F). One thousand images were simulated with a fixed particle brightness of 10 kHz and different particle numbers.

Fig. 2A–C show the dependence of the estimated particle number on the true particle number. In Fig. 2A, the averages are scattered around the true values and do not overlap with them. The medians are closer to the true values than to the averages. In Fig. 2B, the averages are overestimated, and the medians overlap with the true values. In Fig. 2C, the averages are close to the true values. Fig. 2G and 2I show the normalized bias and standard deviation of the particle number; the normalization is divided by the true value. A bias of 0 indicates accurate estimation, and a low standard deviation indicates high-precision estimation. Fig. 2G and 2I show that EB–MAP estimated the particle number with the highest accuracy and precision. The precision of EB–MAP estimation was an order of magnitude higher than that of MoM. Note that the bias and the standard deviation of ML were given by excluding the particle number of infinity; these values are only for reference. Fig. 2D–F show the dependence of the estimated particle brightness on the true particle number. For all the methods, the averages and the medians were close to the true value and were constant. The number of outliers was notably smaller than that estimated for the particle number. Fig. 2H and 2J show the normalized bias and standard deviation of the particle brightness. Fig. 2H indicates that MoM and ML estimated the particle brightness accurately, but EB–MAP overestimated the values. The magnitude of bias on EB–MAP was constant. Fig. 2J indicates that the estimation of EB–MAP was the most precise, that of ML was the second-best, and that of EB–MAP was 1.5 times better than that of MoM. One could consider that either the particle number or particle brightness would be underestimated if the other was overestimated in Fig. 2G and 2H. Although each estimate of MoM and ML satisfies Eq. 18, the average of the estimates does not satisfy such relation (see Supporting Material for details).

These results suggest that EB–MAP is more advantageous than MoM and ML for estimating the particle number. In contrast, the median of the estimates given by MoM and ML would be useful as a representative value. Moreover, Digman et al. (7) and our group (11) applied a spatial median filter to the images of the estimates in previous studies (see Fig. S2.2 in Supporting Material for the results regarding application of median filter). Regarding particle brightness, MoM and ML are advantageous for accurate estimation, but EB–MAP estimates with the highest precision.

Comparison of different laser powers or oligomeric states by simulation

Next, we simulated images imitating measurements with different laser powers or oligomeric states. One thousand images were simulated with a fixed particle number and varying particle brightness. In the simulation of the fixed particle number, we simulated a 2×2 grid-patterned area to demonstrate the applicability of the EB–MAP estimation. The EB–MAP implemented by lognormal prior with gamma hyperprior can be applied even if the particle number changes sharply (see Fig. S1.2 in Supporting Material).

Fig. 3A and 3B show the true and estimated particle numbers given by MoM, ML, and EB–MAP. In the image

with the particle brightness of 20 kHz, the grid pattern was observed clearly for all the methods. In the images with lower particle brightness of 10 and 5 kHz, many outliers appeared in the MoM and ML methods. However, outliers were very small in number, and the edge of the grid pattern was stored, in the case of the EB–MAP method. Fig. 3I and 3K show the normalized bias and standard deviation of the particle number, respectively (see Fig. S3.1 in Supporting Material for box plot). As seen from Fig. 3I, MoM estimated unstably, and sometimes overestimated and underestimated. Further, ML markedly overestimated at lower particle brightness; EB–MAP estimated with a bias of 0 for a particle brightness of over 7.5 kHz and underestimated for a particle brightness of less than 7.5 kHz. As seen in Fig. 3K, ML and EB–MAP estimated more precisely compared with MoM. The precision of EB–MAP estimation was an order of magnitude better than that of MoM. Fig. 3C–H show the true and estimated particle brightness. Although outliers were fewer in number, MoM and ML sometimes estimated negatively if the true particle brightness was low. Fig. 3J and 3L show the normalized bias and standard deviation of the particle brightness, respectively. As seen from Fig. 3J, MoM and ML estimated accurately, except for a true particle brightness of 2.5 kHz; however, EB–MAP markedly overestimated if the true particle brightness was low. Fig. 3L shows that ML and EB–MAP estimated more precisely compared with MoM. To carefully examine the bias produced by MoM and ML, we performed another simulation with a particle brightness of less than 5 kHz (see Fig. S3.4 in Supporting Material). The results showed that MoM underestimated and ML overestimated, if the true particle brightness was low. The magnitude of bias of ML was smaller than that of EB–MAP.

Experimental comparison of different concentrations

To demonstrate the applicability of ML and EB–MAP, we experimentally obtained images of the EGFP solution and analyzed them. In the previous simulations, we simulated the ideal photon counts based on Neyman type A distribution. However, the effect of the dead time on photon detectors cannot be neglected in actuality. We analyzed the images using MoM, ML, and EB–MAP, which can be applied to dead-time-affected photon counts (see Fig. S4.3 in Supporting Material for results without correction for dead time). For analyses based on MoM, we adopted the TD–N&B analysis (11), which does not require correction for dead time. This method is based on covariance and fluorescence intensity estimation; the covariance is not affected by dead time. Although the fluorescence intensity is affected by dead time, we assume that the effect is negligibly small in our measurements. This effect has been previously evaluated by Hillesheim et al. (29). As a control for N&B analysis, FCS measurements were also performed (see Fig. S4.4 in Supporting Material). We prepared different concentrations of EGFP using phosphate-buffered saline (pH 7.4). The average of fluorescence intensity increased with the concentration; we plotted the averages in the *x*-axis. It can be expected that increasing the concentration will increase the particle number, but the particle brightness will remain constant.

Fig. 4A shows the dependence of the average particle number on the average of fluorescence intensity (see Fig. S4.1 in Supporting Material for box plot) and fitted lines. Each line shows an increase in particle number (see Table S4.3 in Supporting Material for details on parameters of the lines). For MoM, the averages were scattered around the fitted line. For ML, the averages were closer to the line, but a few were away from the line at high concentration. For EB–MAP, all the symbols of the average overlapped with the line. Fig. 4B shows the dependence of the average particle brightness on the average of the fluorescence intensity and fitted lines. For all the methods, the averages were close to the fitted line and showed a constant particle brightness. The particle brightness was the highest for EB–MAP and second-highest for ML. The magnitude relationship of particle brightness between MoM, ML, and EB–MAP was similar to that of the simulated result for low particle brightness (see Fig. S3.4 in Supporting Material). Fig.

4C and 4D show the standard deviations of the particle number and particle brightness, respectively. The ML and EB–MAP estimated more precisely compared with MoM. The precision of EB–MAP estimation was an order of magnitude better for particle number and 1.5 times better for particle brightness than those of MoM. These results are consistent with the simulated results.

Experimental comparison of different laser powers

Next, we obtained images of the EGFP solution with different laser powers and analyzed them. As a control, FCS measurements were also performed (see Fig. S5.3 in Supporting Material). It can be expected that increasing the laser power will increase the particle brightness, but the particle number will remain constant.

Fig. 5A shows the dependence of average particle number on the laser power (see Fig. S5.1 in Supporting Material for box plot). For MoM, the averages had a large variation and were not constant. For ML, the averages increased roughly and seemed to become constant at high laser power, but did not increase monotonically. For EB–MAP, the averages increased and saturated at high laser power. The dotted line was arbitrarily drawn with a slope of 0 and an intercept of 53.1, which is an average of the first three largest values (i.e., the highest average, second-highest average, and third-highest average). Fig. 5B shows the dependence of the average particle brightness on the laser power. For all the methods, the averages were close to the fitted line and increased (see Table S5.3 in Supporting Material for details on parameters of the lines). For MoM, the lines had an intercept of nearly 0. In contrast, for ML and EB–MAP, although the fitted line characterized the averages precisely, the lines had positive intercepts. Fig. 5C and 5D show the standard deviations of the particle number and particle brightness, respectively. Both ML and EB–MAP estimated more precisely than MoM. The precision of EB–MAP estimation was an order of magnitude better for particle number and 1.5–2 times better for particle brightness than those of MoM. These results are consistent with the simulated results.

Experimental comparison of EGFP tandem oligomers

Finally, we prepared HeLa cells expressing the EGFP monomer, dimer, and trimer separately. The dimer and trimer are EGFP tandem-oligomers, and have flexibly linked two and three EGFP units, respectively. Increasing the EGFP unit will increase the particle brightness. We obtained their images and analyzed them. For quantification, we placed regions of interest (ROIs) of the size 16×16 in the nucleus and cytoplasm, and estimated the averages. Additionally, FCS measurements were also performed as a control (see Fig. S6.4 in Supporting Material).

Fig. 6A shows the fluorescence intensity of a cell expressing EGFP monomer, and Fig. 6B shows the particle number (see Fig. S6.1 and S6.2 in Supporting Material for other results). For MoM and ML, the outline of the nuclear membrane and cellular structure is not clear due to the presence of many outliers. On the other hand, for EB–MAP, there are no outliers and the contrast between the fluorescence intensity and particle number seems similar. The histogram of the particle number in the cytoplasm shows that EB–MAP suppressed the appearance of larger values (see Fig. S6.3 in Supporting Material). Fig. 6C–E show the dependence of the average particle brightness on the number of EGFP units, and Fig. 6F shows the normalized particle brightness and fold change in the particle brightness in the cytoplasm; the normalization is divided by the average of the average particle brightness of the monomer. The fold change in the particle brightness is the normalized average of averages. For MoM, increasing the number of EGFP units increased the average of averages in cytoplasm, and the average did not clearly increase from EGFP dimer to trimer in the nucleus. The fold change in particle brightness did not correspond with the number of EGFP units. The results of FCS were similar to those of MoM. All these results are consistent with the results of a

previous study (11). For ML and EB–MAP, the averages were higher, and the fold changes were smaller than those of MoM. To examine the cause of the decreasing fold change, we subtracted the intercept obtained in Fig. 5B from the average particle brightness (the intercept is 2.80 and 6.62 for ML and EB–MAP, respectively), and calculated the fold change (indicated by "+" in Fig. 6F). The corrected fold changes of ML and EB–MAP were recovered and found to be equivalent to those of MoM.

DISCUSSION

Thus far, we have demonstrated that EB–MAP can estimate precisely. In our statistical model, we did not include a model describing the point spread function (PSF) and scanning to reduce the computational cost. The spatial intensity distribution of the excitation light is described by PSF, and the position of a fluorescent particle in PSF affects the particle brightness. Additionally, scanning changes the position of the fluorescent particles in PSF. In a photon counting histogram (PCH) (21), the Gaussian–Lorentzian distribution and 3D Gaussian distribution are used for two-photon excitation and one-photon excitation (21), respectively. Including a model for PSF requires the calculation of convolution. Our algorithm for EB–MAP requires iterative computation for numerical integration; the iterative computation is required for each pixel. To prevent any further increase in computational cost, we did not include the model. Nevertheless, the dependence of the estimated particle number and particle brightness on the sample concentration and laser power corresponded well with the theoretically expected relationship (see Fig. 4 and 5). These results suggest that our method characterized the intensity fluctuation comparatively. However, these results are not absolute estimations, and the estimates could be affected by a shape factor of the PSF described in PCH (21).

In the construction of prior distribution, we assumed lognormal distribution for the particle number; this assumption limits the particle number. In contrast, we assumed uniform distribution for the particle brightness; this assumption does not limit the particle brightness. Another construction of prior distribution is possible, i.e., limiting both the parameters. Such a prior distribution would be useful in further improving the precision. However, this construction increases the number of hyperparameters to be optimized simultaneously, and consequently increases the computational cost. Thus, we simplified the prior distribution and limited only the particle number. In future studies, a prior distribution limiting both the parameters would be required. Our assumption in the prior distribution ignored the distribution of particle brightness and the correlation between the particle number and particle brightness. However, the particle number and particle brightness correlate negatively on the likelihood function. Ignoring the particle brightness in the prior distribution would result in omitted-variable bias (30) (Chapter 3.3), which could have been a possible cause for the overestimated particle brightness in EB–MAP (Fig. 3J). To construct a prior distribution limiting both the parameters, an orthogonal parameterization (31) would be useful to eliminate the correlation of the parameters.

In fluorescence imaging and N&B analysis, the background intensity is a problem. For example, dark count, stray light, and autofluorescence would be sources of background intensity. Dark count and stray light can be corrected by implementing an additional probability distribution such as Poisson distribution, and by estimating the intensity of the background by a reference measurement. However, the correction for autofluorescence is challenging, because the intensity of autofluorescence differs depending on the position in cell and the cellular structure. We assumed that the effect of background intensity can be suppressed by increasing the fluorescence intensity from the target particles. We measured cells with fluorescence intensity, to the maximum extent possible; therefore, we did not perform corrections for background in this research (see Materials and Methods in Supporting

Material).

We simulated photon count images with different particle numbers (Fig. 2) and particle brightness (Fig. 3), and evaluated the bias and standard deviation. The evaluation of the bias and standard deviation suggested the following. (a) For estimating the particle number, EB–MAP would be better to improve the accuracy and precision; however, EB–MAP underestimates the particle number if the true particle brightness is low. (b) MoM and ML often cause outliers, which skews the average. The median would be useful to characterize the distribution instead. (c) For estimating the particle brightness, the choice of estimator would change depending on the purpose of the analyst. MoM would be a better choice if the analyst expects estimation with less bias. On the other hand, ML and EB–MAP would be better if the analyst expects precise estimation, and already knows that the true particle brightness is constant or a correction for the bias is available.

We applied these methods to the images of EGFP solution with different concentrations (Fig. 4) and laser powers (Fig. 5). We analyzed the images with the models considering the dead-time effect; considering this effect enabled recovery of the behavior of the parameters on different concentrations (see Fig. S4.4 in Supporting Material for results without correction). This suggests that the consideration of dead time is essential.

In the estimations of particle number with different laser powers using EB−MAP (Fig. 5), the particle number increased with the increasing laser power and saturated at the highest laser power. Considering the simulated results, the saturated value of 53.1 would be an unbiased estimation, although the true particle number is unknown in the experiments. However, decreasing the laser power below 1.6% decreased the estimates. Although experiments with different concentrations (Fig. 4) were conducted with a laser power of less than 1.6%, increasing the concentration increased the particle number linearly. This suggests that an underestimated particle number would be comparable, if the true particle brightness is the same.

In the estimation of particle brightness with different laser powers (Fig. 5), EB–MAP estimated the highest average of particle brightness, and ML and MoM estimated the second- and third-highest averages, respectively. These estimates were characterized well by lines, and ML and EB–MAP had clear positive intercepts. This result indicates that doubling or tripling the true particle brightness does not proportionally increase the particle brightness estimated by ML and EB–MAP. Therefore, in the experiments with EGFP tandem oligomers, the fold change in particle brightness by ML and EB–MAP decreased compared with that of MoM (Fig. 6F). We calculated the fold change again by subtracting the intercept (indicated by "+": ML (+) and EB–MAP (+) in Fig. 6F). This correction recovered the fold change in particle brightness by ML and EB–MAP to be equivalent to that of MoM. This result implies that although ML and EB–MAP overestimate the particle brightness, they could be useful for relative quantification of particle brightness. The theoretical behavior of the estimated particle brightness was not investigated in detail in this study. Further studies are required for robust correction of the fold change. We performed simulations to investigate the origin of the positive intercept (see Fig. S5.4 in Supporting Material). The simulation results showed that the intercept decreased with the increasing number of images. The origin of the positive intercept would be the insufficient number of images at low particle brightness. Subtracting the intercept would compensate when sufficient number of images is not available. Further, the number of EGFP units did not correspond with the fold change obtained by MoM (Fig. 6C); this result is the same as that of FCS (see Fig. S6.4 in Supporting Material) and consistent with that of a previous study (11). These results suggest the presence of a non-fluorescent state of EGFP. There are several possible explanations for this phenomenon. One could be the photophysical processes, such as long-lived dark states (32) and photobleaching (33), and another could be the chromophore formation (protein maturation and incorrect folding) (34–36). To estimate the number of EGFP units

accurately, a simple correction method was proposed for the non-fluorescent state (35, 37). For error analyses on the fold change, see the sections in page 33–42, Supporting Material.

CONCLUSION

We applied ML and EB–MAP to N&B analysis to accurately and precisely estimate the particle number and particle brightness, which reflect the concentration and oligomeric state, respectively, of a fluorescently labeled protein in a cell. In the construction of EB–MAP, we effectively utilized the information of the surrounding pixels by assuming lognormal prior and gamma hyperprior. To extend the feasibility of our analysis, we combined the double-detector system achieved by a half mirror (11) and the correction for the dead time of photon detectors. We demonstrated the feasibility, accuracy, and precision of our method by simulations and experiments. The results showed that EB–MAP can be applied even if the particle number of the surrounding pixels changes sharply; further, EB–MAP estimated with better precision compared with that of the conventional method. Although EB–MAP overestimated the particle brightness, a simple correction recovered the fold change in particle brightness comparable to the conventional method. Our method (EB–MAP–N&B) recognizes the changes in parameters sensitively.

The N&B analysis is advantageous for monitoring the spatial distribution of the concentration and oligomeric state in cells. The measurement in this method is performed using confocal laser scanning microscopy. Our method has a wide range of applications in the field of fluorescence imaging. Furthermore, our method would contribute to the understanding of the dynamic processes in oligomerization and protein aggregation in cells.

To our knowledge, this is the first study that applies Bayesian statistics to N&B analysis, and we revealed the great potential of Bayesian statistics. The methods reported herein will open up avenues for further research in this field. In this study, although we mainly focused on the pair of parameters that maximizes the joint posterior distribution, other choices of estimators are also possible. The MAP estimate can be determined by maximizing the marginal distribution of the joint posterior distribution. Additionally, the expected a posteriori (EAP) estimate can also be determined. Evaluating the accuracy and precision of other estimators would widen the choice of estimators. We further note that EB–MAP can be applied to other FFS techniques, namely, scanning FCS (38) and imaging FCS (2, 39), to improve their accuracy and precision. These methods record the spatial distribution of fluorescence fluctuation, as with N&B analysis. Therefore, expecting a similarity between parameters at spatially close positions would be reasonable. The spatial similarity of parameters is typically not assumed if the parameters are estimated by analyzing the temporal fluctuation at a position. We demonstrated that assuming the spatial similarity is useful to effectively extract the information contained in fluorescence images.

SUPPORTING MATERIAL

Theoretical derivations, materials and methods, and supplemental data are available at (URL).

AUTHOR CONTRIBUTIONS

R. F. designed and conducted the research, analyzed data, and wrote the manuscript; J. Y. and M. K. supervised the project.

ACKNOWLEDGMENT

SUPPORTING CITATIONS

References (40–53) appear in the Supporting Material.

REFERENCE

1. Youker, R.T., and H. Teng. 2014. Measuring protein dynamics in live cells: protocols and practical considerations for fluorescence fluctuation microscopy. *J. Biomed. Opt.* 19:090801.

2. Bag, N., and T. Wohland. 2014. Imaging Fluorescence Fluctuation Spectroscopy: New Tools for Quantitative Bioimaging. *Annu. Rev. Phys. Chem.* 65:225–248.

3. Migueles-Ramirez, R.A., A.G. Velasco-Feliz, R. Pinto-Camara, C.D. Wood, and A. Guerrero. 2017. Fluorescence fluctuation spectroscopy in living cells. *Microsc. imaging Sci. Pract. approaches to Appl. Res. Educ.* 138–151.

4. Elson, E.L., and D. Magde. 1974. Fluorescence correlation spectroscopy. I. Conceptual basis and theory. *Biopolymers*. 13:1–27.

5. Krmpot, A.J., S.N. Nikolić, M. Vitali, D.K. Papadopoulos, S. Oasa, P. Thyberg, S. Tisa, M. Kinjo, L. Nilsson, W.J. Gehring, L. Terenius, R. Rigler, and V. Vukojević. 2015. Quantitative confocal fluorescence microscopy of dynamic processes by multifocal fluorescence correlation spectroscopy. In: Advanced Microscopy Techniques IV; and Neurophotonics II. OSA, Washington, D.C. p. 95360O.

6. Yamamoto, J., S. Mikuni, and M. Kinjo. 2018. Multipoint fluorescence correlation spectroscopy using spatial light modulator. *Biomed. Opt. Express*. 9:5881.

7. Digman, M.A., R. Dalal, A.F. Horwitz, and E. Gratton. 2008. Mapping the Number of Molecules and Brightness in the Laser Scanning Microscope. *Biophys. J.* 94:2320–2332.

8. Qian, H., and E.L. Elson. 1990. On the analysis of high order moments of fluorescence fluctuations. *Biophys. J.* 57:375–380.

9. Qian, H., and E.L. Elson. 1990. Distribution of molecular aggregation by analysis of fluctuation moments. *Proc. Natl. Acad. Sci.* 87:5479–5483.

10. Saleh, B. 1978. Photoelectron statistics with applications to spectroscopy and optical communication. Springer-Verlag Berlin Heidelberg GmbH, .

11. Fukushima, R., J. Yamamoto, H. Ishikawa, and M. Kinjo. 2018. Two-detector number and brightness analysis reveals spatio-temporal oligomerization of proteins in living cells. *Methods*. 140–141:161–171.

12. Strey, H.H. 2019. Estimation of parameters from time traces originating from an Ornstein-Uhlenbeck process. *Phys. Rev. E*. 100:062142.

13. Jazani, S., I. Sgouralis, O.M. Shafraz, M. Levitus, S. Sivasankar, and S. Pressé. 2019. An alternative framework for fluorescence correlation spectroscopy. *Nat. Commun.* 10:3662.

14. Santra, K., J. Zhan, X. Song, E.A. Smith, N. Vaswani, and J.W. Petrich. 2016. What Is the Best Method to Fit Time-Resolved Data? A Comparison of the Residual Minimization and the Maximum Likelihood Techniques As Applied to Experimental Time-Correlated, Single-Photon Counting Data. *J. Phys. Chem. B*. 120:2484–2490.

15. Santra, K., E.A. Smith, J.W. Petrich, and X. Song. 2017. Photon Counting Data Analysis: Application of the Maximum Likelihood and Related Methods for the Determination of Lifetimes in Mixtures of Rose Bengal and Rhodamine B. *J. Phys. Chem. A*. 121:122–132.

16. Shenton, L.R. 1949. On the efficiency of the method of moments and Neyman's type A distribution. *Biometrika*. 36:450–454.

17. Shenton, L.R., and K.O. Bowman. 1967. Remarks on Large Sample Estimators for Some Discrete Distributions. *Technometrics*. 9:587–598.

18. Galindo Garre, F., and J.K. Vermunt. 2006. Avoiding Boundary Estimates in Latent Class Analysis by Bayesian Posterior Mode Estimation. *Behaviormetrika*. 33:43–59.

19. Allman, E., H.B. Cervantes, S. Hosten, K. Kubjas, D. Lemke, J. Rhodes, and P. Zwiernik. 2019. Maximum likelihood estimation of the Latent Class Model through model boundary decomposition. *J. Algebr. Stat.* 10:51–84.

20. Mandel, L. 1958. Fluctuations of Photon Beams and their Correlations. *Proc. Phys. Soc.* 72:1037–1048.

21. Chen, Y., J.D. Müller, P.T.C. So, and E. Gratton. 1999. The Photon Counting Histogram in Fluorescence Fluctuation Spectroscopy. *Biophys. J.* 77:553–567.

22. Hillesheim, L.N., and J.D. Müller. 2005. The dual-color photon counting histogram with non-ideal photodetectors. *Biophys. J.* 89:3491–3507.

23. Neyman, J. 1939. On a new class of "contagious" distributions, applicable in entomology and bacteriology. *Ann. Math. Stat.* 10:35–57.

24. Adelson, R.. 1966. Compound Poisson Distributions. *Oper. Res. Soc.* 17:73–75.

25. Hendrix, J., W. Schrimpf, M. Höller, and D.C. Lamb. 2013. Pulsed Interleaved Excitation Fluctuation Imaging. *Biophys. J.* 105:848–861.

26. Bishop, C.M. 2006. Pattern Recognition and Machine Learning. Springer, Germany.

27. Gelman, A., J. Carlin, H. Stern, and D. Rubin. 2004. Bayesian data analysis. 3rd ed. Chapman & Hall/CRC, UK.

28. Chung, Y., S. Rabe-Hesketh, V. Dorie, A. Gelman, and J. Liu. 2013. A Nondegenerate Penalized Likelihood Estimator for Variance Parameters in Multilevel Models. *Psychometrika*. 78:685–709.

29. Hillesheim, L.N., and J.D. Müller. 2003. The Photon Counting Histogram in Fluorescence Fluctuation Spectroscopy with Non-Ideal Photodetectors. *Biophys. J.* 85:1948–1958.

30. Wooldridge, J.M. 2009. Introductory Econometrics: A Modern Approach. 5th ed. South-Western, Cengage Learning, USA.

31. Willmot, G.E. 1988. Parameter Orthogonality for a Family of Discrete Distributions. *J. Am. Stat. Assoc.* 83:517–521.

32. Widengren, J., Ü. Mets, and R. Rigler. 1999. Photodynamic properties of green fluorescent proteins investigated by fluorescence correlation spectroscopy. *Chem. Phys.* 250:171–186.

33. Hur, K.-H., P.J. Macdonald, S. Berk, C.I. Angert, Y. Chen, and J.D. Mueller. 2014. Quantitative Measurement of Brightness from Living Cells in the Presence of Photodepletion. *PLoS One*. 9:e97440.

34. Balleza, E., J.M. Kim, and P. Cluzel. 2018. Systematic characterization of maturation time of fluorescent proteins in living cells. *Nat. Methods*. 15:47–51.

35. Dunsing, V., M. Luckner, B. Zühlke, R.A. Petazzi, A. Herrmann, and S. Chiantia. 2018. Optimal fluorescent

protein tags for quantifying protein oligomerization in living cells. *Sci. Rep.* 8:10634.

36. Foo, Y.H., N. Naredi-Rainer, D.C. Lamb, S. Ahmed, and T. Wohland. 2012. Factors affecting the quantification of biomolecular interactions by fluorescence cross-correlation spectroscopy. *Biophys. J.* 102:1174–1183.

37. Vámosi, G., N. Mücke, G. Müller, J.W. Krieger, U. Curth, J. Langowski, and K. Tóth. 2016. EGFP oligomers as natural fluorescence and hydrodynamic standards. *Sci. Rep.* 6:33022.

38. Petrášek, Z., and P. Schwille. 2008. Scanning Fluorescence Correlation Spectroscopy. In: Single Molecules and Nanotechnology. Springer, Berlin, Heidelberg, . pp. 83–105.

39. Kannan, B., J.Y. Har, P. Liu, I. Maruyama, J.L. Ding, and T. Wohland. 2006. Electron Multiplying Charge-Coupled Device Camera Based Fluorescence Correlation Spectroscopy. *Anal. Chem.* 78:3444–3451.

40. Bédard, G. 1967. Dead-time corrections to the statistical distribution of photoelectrons. *Proc. Phys. Soc.* 90.

41. Ackermann, J., and H. Hogreve. 2010. Small dead-time expansion in counting distributions and moments. *Nucl. Instruments Methods Phys. Res. Sect. A Accel. Spectrometers, Detect. Assoc. Equip.* 614:297–302.

42. Oura, M., J. Yamamoto, H. Ishikawa, S. Mikuni, R. Fukushima, and M. Kinjo. 2016. Polarization-dependent fluorescence correlation spectroscopy for studying structural properties of proteins in living cell. *Sci. Rep.* 6:31091.

43. Pack, C., K. Saito, M. Tamura, and M. Kinjo. 2006. Microenvironment and Effect of Energy Depletion in the Nucleus Analyzed by Mobility of Multiple Oligomeric EGFPs. *Biophys. J.* 91:3921–3936.

44. Takahasi, H., and M. Mori. 1973. Double exponential formulas for numerical integration. *Publ. Res. Inst. Math. Sci.* 9:721–741.

45. Müller, C.B., A. Loman, V. Pacheco, F. Koberling, D. Willbold, W. Richtering, and J. Enderlein. 2008. Precise measurement of diffusion by multi-color dual-focus fluorescence correlation spectroscopy. *Europhys. Lett*. 83:46001.

46. Culbertson, C.T., S.C. Jacobson, and J. Michael Ramsey. 2002. Diffusion coefficient measurements in microfluidic devices. *Talanta*. 56:365–73.

47. Amrhein, V., S. Greenland, and B. McShane. 2019. Scientists rise up against statistical significance. *Nature*. 567:305–307.

48. Johnson, D.H. 1999. The Insignificance of Statistical Significance Testing. *J. Wildl. Manage.* 63:763.

49. Lemoine, N.P. 2019. Moving beyond noninformative priors: why and how to choose weakly informative priors in Bayesian analyses. *Oikos*. 128:912–928.

50. Gelman, A. 2006. Prior distributions for variance parameters in hierarchical models (comment on article by Browne and Draper). *Bayesian Anal.* 1:515–534.

51. Polson, N.G., and J.G. Scott. 2012. On the Half-Cauchy Prior for a Global Scale Parameter. *Bayesian Anal.* 7:887–902.

52. R Core Team. 2020. R: A language and environment for statistical computing. R Foundation for Statistical Computing, Vienna, Austria. https://www.r-project.org/.

53. Stan Development Team. 2020. RStan: the R interface to Stan. http://mc-stan.org/.

FIGURE 1

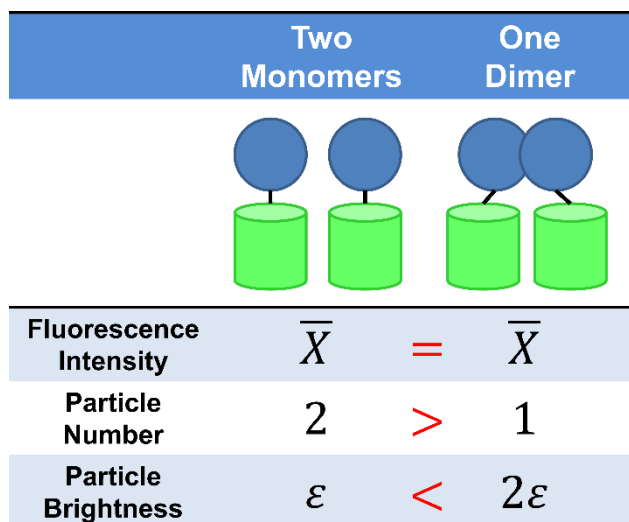|	Two Monomers		One Dimer
Fluorescence Intensity	$\overline{X}$	=	$\overline{X}$
Particle Number	2	>	1
Particle Brightness	ε	<	2ε

FIGURE 1: Reflection of oligomeric state by particle brightness

Fluorescent protein (green cylinder), two fluorescently labeled monomers, and one dimer. Fluorescence intensity of the monomers and the dimer are given by $\overline{X}$ (the overline represents average). In the dimerization, the particle number reduces by half, and the particle brightness doubles.

FIGURE 2
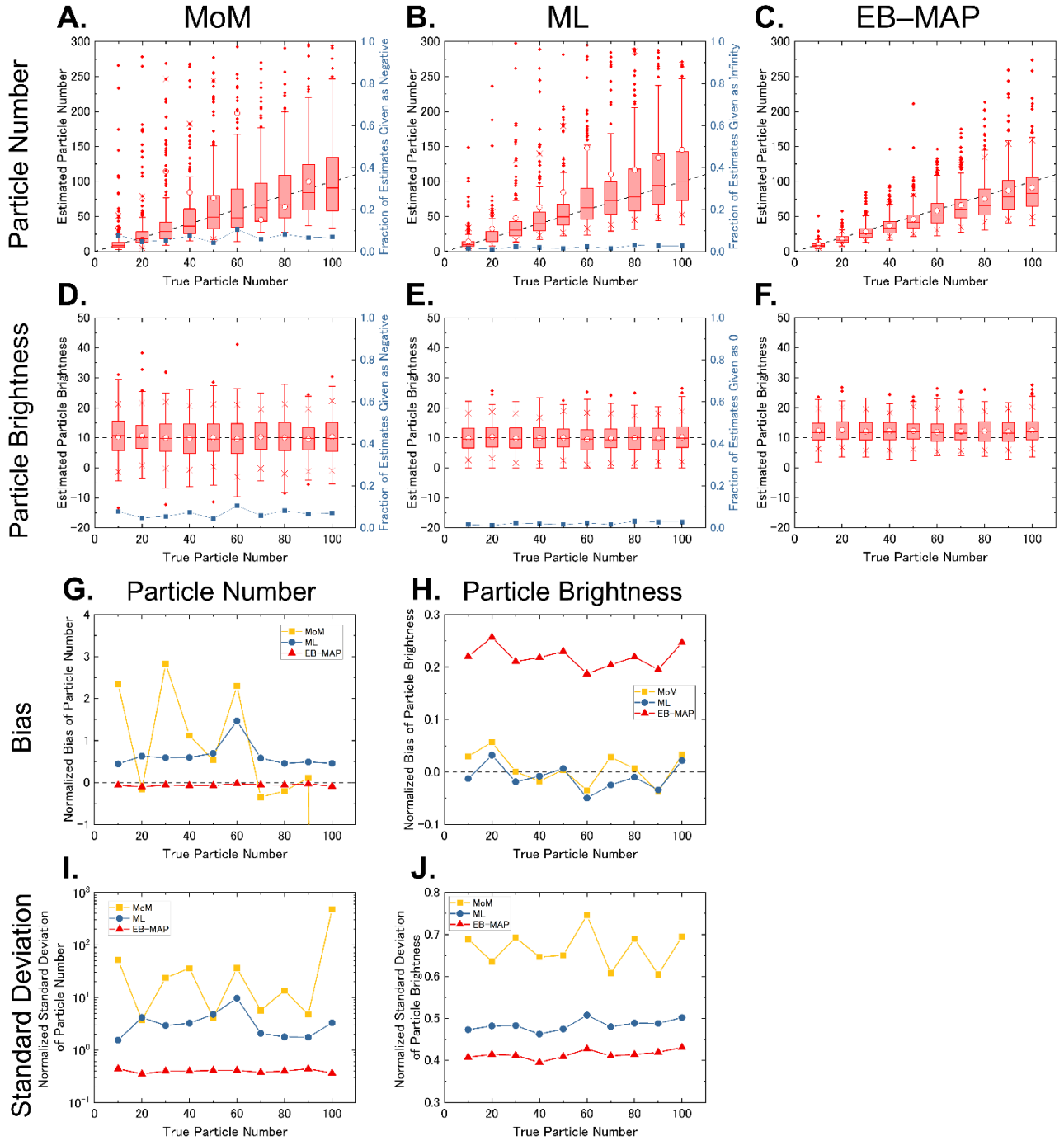
FIGURE 2: Simulations with different particle numbers

One thousand images were simulated with a fixed particle brightness of 10 kHz and different particle numbers, and analyzed by MoM (A, D), ML (B, E), and EB–MAP (C, F). (A, B, C) Dependence of the estimated particle number on true particle number. Dashed lines represent the true value. In the box plot, open circle: average, box: interval between 25th and 75th percentiles, central bar: median, diamonds: outliers, crosses: 5th and 95th percentiles, and the error bars are minimum and maximum points without outliers. Fig. 2A and 2B contain numerous outliers, which are shown in an enlarged view (see Fig. S2.1 in Supporting Material for broad view). In MoM and ML estimations, estimates are sometimes out of the parameter space; the fraction of estimates outside the parameter space is shown on the right axes. (D, E, F) Dependence of the estimated particle brightness [kHz] on true particle number. A fraction of estimates outside the parameter space is shown. (G–J) Normalized bias and standard deviation are shown for particle numbers (G, I) and particle brightness (H, J).
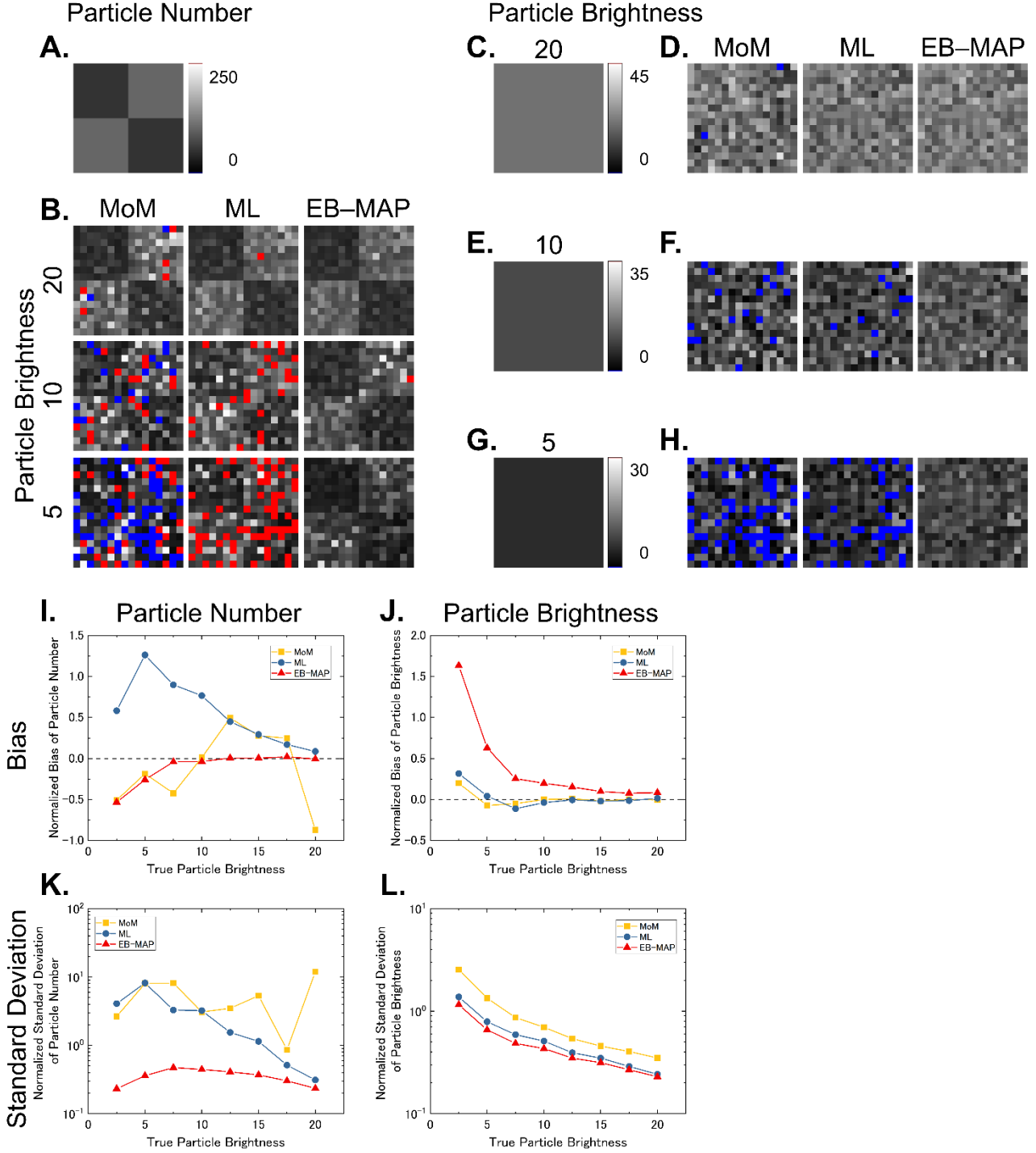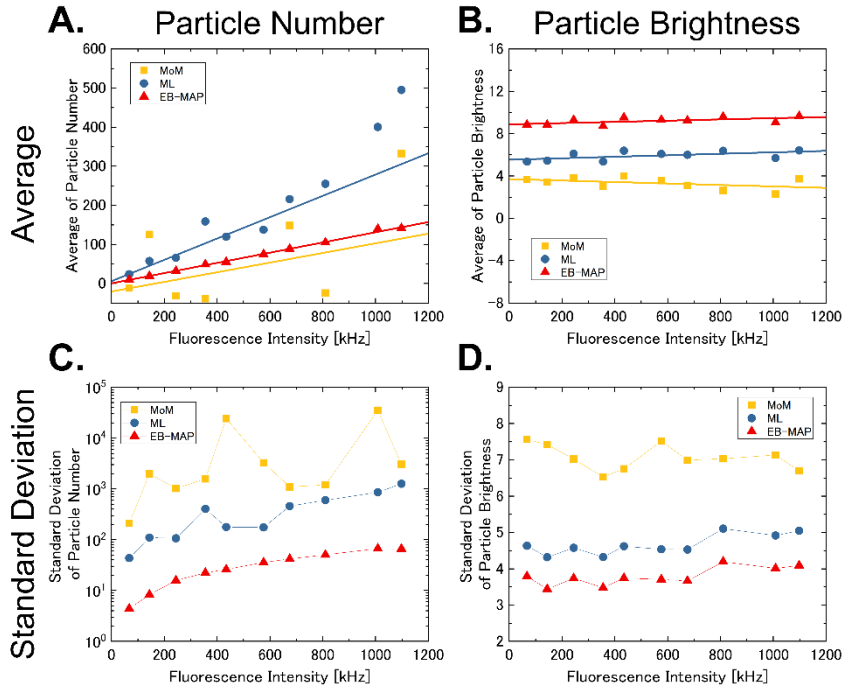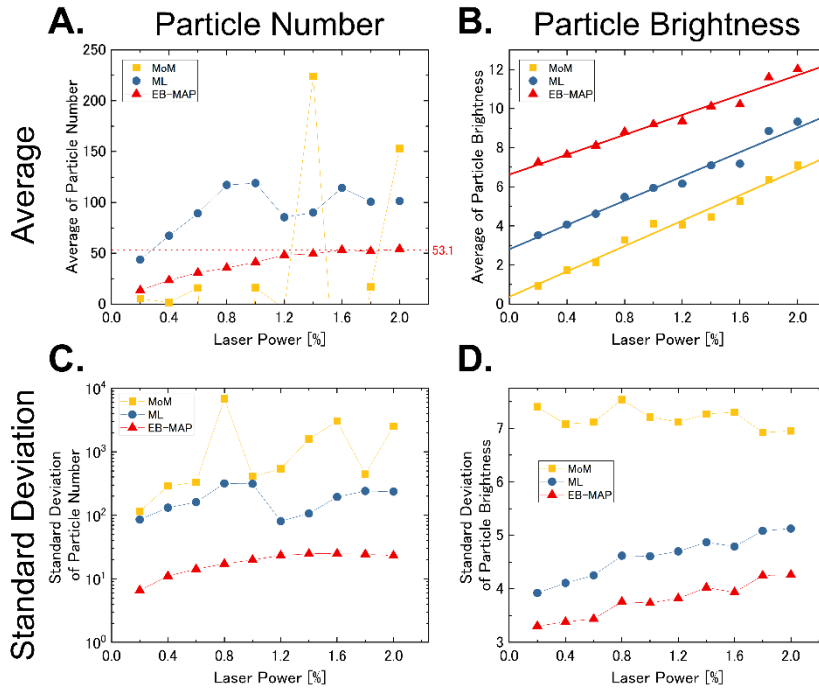
FIGURE 3

FIGURE 3: Simulations with different particle brightness on grid-patterned image

One thousand images were simulated with a fixed particle number and different particle brightness. The particle number has a 2×2 grid-patterned area, in which each pixel has 50 or 100 particles. (A) True image for particle number. (B) Estimated images for the particle number given by MoM, ML, and EB–MAP under different particle brightness [kHz]. The brightness and contrast of the images are the same between A and B. The pixels below the range are colored in blue, and those beyond the range are colored in red. (C, E, G) True images for the particle brightness of 20, 10, and 5 kHz, respectively. (D, F, H) Estimated images for particle brightness [kHz]. The brightness and contrast of the images are the same between C and D, E and F, and G and H. (I–L) Normalized bias and standard deviation for a true particle number of 100 particles (I, K) and particle brightness (J, L).

FIGURE 4

FIGURE 4: Experiments on EGFP solution with different concentrations

Dependence of average and standard deviation on the concentration for particle number (A, C) and particle brightness [kHz] (B, D). Fluorescence intensity is plotted on the x-axis, instead of the concentration. The solid lines in A and B are fitted lines obtained by the weighted least squares method.

FIGURE 5

FIGURE 5: Experiments on EGFP solution with different laser power

Dependence of average and standard deviation on the laser power for particle number (A, C) and particle brightness [kHz] (B, D). The dotted line in A was arbitrarily drawn with a slope of 0 and an intercept of 53.1. The solid lines in B are fitted lines obtained by the weighted least squares method.
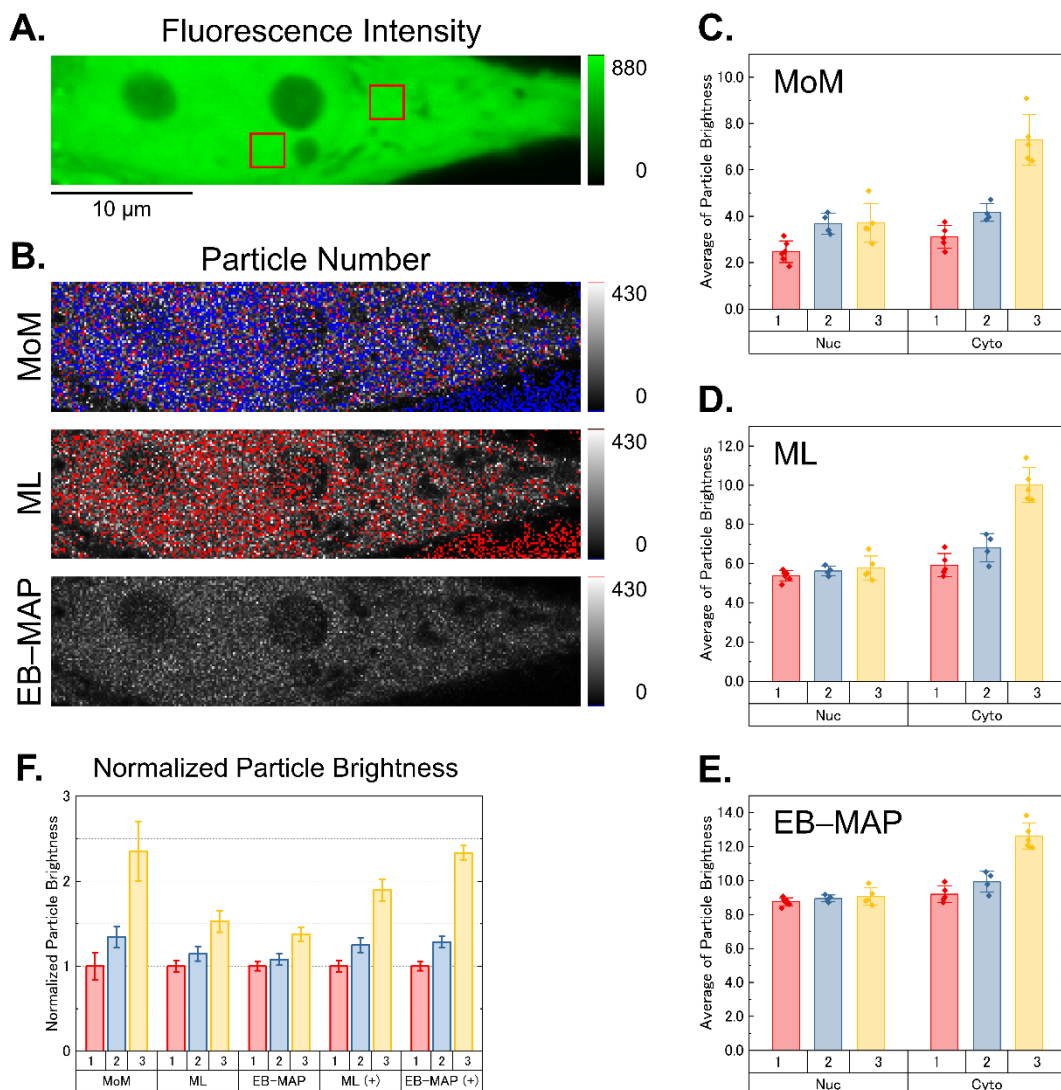
FIGURE 6

FIGURE 6: Experiments on EGFP tandem oligomers in cells

(A) Fluorescence intensity [kHz] of a cell expressing an EGFP monomer. The red squares are regions of interest (ROIs) placed in the nucleus and cytoplasm. (Please see the digital version of this figure because printed version could seem different.) (B) Estimated images for particle number analyzed by MoM, ML, and EB–MAP. The pixels below the range are colored in blue, and those beyond the range are colored in red. (C–E) Dependence of average particle brightness [kHz] on the number of EGFP units in the nucleus (Nuc) and cytoplasm (Cyto). Dots: sample average of particle brightness in the ROIs, bar: average of the averages, and error bar: sample standard deviation of the averages. (F) Normalized particle brightness in the cytoplasm. Bar: fold change in particle brightness (sample average of the normalized average particle brightness), error bar: sample standard deviation of the normalized average particle brightness. The symbol "+" represents the correction for particle brightness by subtracting the intercept in Fig. 5B.